American Mineralogist, Volume 82, pages 962–978, 1997

Structure of synthetic monoclinic Na-rich birnessite and hexagonal birnessite: II. Results from chemical studies and EXAFS spectroscopy

Ewen Silvester,[1,†] Alain Manceau,[1,*] and Victor A. Drits[2]

[1]Environmental Geochemistry Group, LGIT-IRIGM, University of Grenoble and CNRS, 38041 Grenoble Cedex 9, France
[2]Geological Institute of the Russian Academy of Sciences, 7 Pyzhevsky prospekt, 109017 Moscow, Russia

Abstract

Solution chemical techniques were used to study the conversion of synthetic Na-rich buserite (NaBu) to hexagonal (H^+-exchanged) birnessite (HBi) at low pH. The low-pH reaction is broadly characterized by the exchange of structural Na^+ with solution H^+ and the partial loss of Mn^{2+} to the aqueous phase. The desorption of Na^+ in two temporally distinct steps indicates the existence of two types of binding sites for this cation. Mn^{2+} appears to originate from a partial disproportionation of Mn^{3+} in the NaBu layers, according to the sequence

$$Mn^{3+}_{layer} + Mn^{3+}_{layer} \rightarrow Mn^{4+}_{layer} + Mn^{2+}_{layer} \rightarrow Mn^{4+}_{layer} + \text{Vacancy} + Mn^{2+}_{aq}.$$

EXAFS measurements on Na-rich birnessite (NaBi) show that this mineral is primarily a layered structure formed by edge-sharing MnO_6 octahedra, with no evidence for triple-corner (TC) sharing Mn. HBi is significantly different with strong evidence for TC-sharing Mn and therefore layer vacancies. The relative numbers of edge (E)-sharing and TC-sharing neighbors determined from EXAFS measurements on HBi is consistent with SAED results (Drits et al. 1997), which suggest that the layer vacancies are restricted to every third row of Mn cations, with 50% of the Mn sites along these rows vacant. The density of vacancies in the entire layer is therefore one in six of layer Mn sites. Polarized EXAFS measurements on orientated films of NaBi and HBi confirm the absence of TC-sharing Mn in NaBi and indicate that Mn adsorbed at layer vacancy sites in HBi at pH 4 is dominantly Mn^{3+}. The intensity of the TC-sharing contribution to the Mn EXAFS spectra of HBi samples increases with increasing pH from pH 2 to 5, and supports a mechanism of formation involving both the direct migration of layer Mn^{3+} to interlayer TC-sharing positions and re-adsorption of Mn^{2+} from solution onto layer vacancy sites. The migration of Mn^{3+} cations into the interlayer releases the steric strain associated with the Jahn-Teller distortion of these octahedra. This model of the NaBu-to-HBi conversion explains the transformation from orthogonal to hexagonal layer symmetry, respectively, as reported by Drits et al. (1997).

Analysis of the Zn EXAFS spectrum of Zn^{2+}-exchanged birnessite shows that Zn^{2+} also occupies TC-sharing positions at layer vacancy sites. The results of this study strongly suggest that lattice cation vacancies are of critical importance in adsorption and electron transfer processes occurring at the surface of this mineral.

Introduction

Hydrous manganese oxides (HMO) play a pivotal role in the redox and adsorption processes that occur in soil, groundwater, oceanic, and aquatic systems (e.g., Krauskopf 1957; McKenzie 1967; Werhli et al. 1995). In laboratory-based studies of such processes, synthetically prepared manganese oxides are commonly used as model materials to avoid the inherent complexity of natural materials (e.g., Gray and Malati 1979a, 1979b; Catts and Langmuir 1986; McKenzie 1980). Synthetic buserite and birnessite, being of mixed Mn valency and generally disordered in nature, mimic the essential features of natural layered HMO and have been used as model manganese oxide materials. Recent electron transfer studies performed using synthetic Na-rich buserite (Crowther et al. 1983; Xyla et al. 1992; Manceau and Charlet 1992) revealed considerable information on the reaction mechanisms involved, however the relatively poor structural characterization of this mineral remains a principal limitation in understanding these reactions at the atomic level. In particular, a knowledge of the spatial distribution of lower valency states of Mn (Mn^{3+} and Mn^{2+}) as well as

* Author to whom correspondence should be addressed.
† Present address: CSIRO Division of Minerals, Box 312, Clayton South, 3169, Australia.

0003–004X/97/0910–0962$05.00

the abundance and distribution of lattice cation vacancies is required.

Buserite and birnessite can be broadly described as having a layered structure, formed by edge-sharing MnO_6 octahedra. The interlayer region between adjacent layers is occupied by various combinations of cationic species and H_2O according to the particular buserite or birnessite species. For synthetic Na-rich buserite the interlayer region is occupied by Na^+ ions and H_2O. Partial dehydration leads to the formation of the Na-rich birnessite phase and is associated with a change in the interlayer spacing from 10 to 7 Å (Giovanoli 1980), a difference that is approximately equal to the diameter of molecular H_2O (2.8 Å).

Adsorption and redox processes are typically studied under low pH conditions. With the exception of the studies by Giovanoli et al. (1970b, 1980) there has been very few investigations of the structure of the low pH forms of synthetic buserite and birnessite. Chemical analyses show that below pH 7, Na^+ in the solid exchanges for H^+ from solution, whereas structural studies reveal a change in the interlayer spacing from 10 to 7 Å (Giovanoli et al. 1970b). This change in interlayer spacing is similar to that observed between synthetic Na-rich buserite and Na-rich birnessite, although it is reasonable to suppose that at low pH the decrease of the interlayer spacing is at least partly associated with loss of Na^+ from the interlayer. Selected-area electron diffraction (SAED) and X-ray diffraction (XRD) studies of synthetic Na-rich birnessite and H-exchanged birnessite microcrystals show that the high pH to low pH transformation is characterized by a change from a monoclinic unit cell (Post and Veblen 1990; Giovanoli et al. 1970a) to a hexagonal unit cell, as was demonstrated by Drits et al. (1997) and, to some extent, demonstrated previously (Giovanoli et al. 1970b).

The synthetic forms of Na-rich buserite and Na-rich birnessite that were prepared in this study are referred to by the names NaBu and NaBi, respectively. The low pH forms of synthetic buserite and birnessite are all characterized by a 7 Å layer spacing, regardless of whether they are in the form of a suspension or as a dry powder. On the basis of both the similar chemical nature of the low pH forms of synthetic buserite and birnessite and the observation that all are 7 Å hexagonal species, we believe that they are, collectively, most appropriately referred to as hexagonal birnessite (HBi).

In this article, the results from chemical studies of the NaBu to HBi conversion process and extended X-ray absorption fine structure (EXAFS) spectroscopic studies of both NaBi and HBi are presented and discussed in light of the structural observations of Drits et al. (1997). One of the primary aims of these articles is to present structural and chemical models for NaBi and HBi that can be used to assist in the interpretation of the adsorption and electron transfer processes that occur on the surfaces of these minerals.

Experimental description

Preparation of Na-rich buserite and Na-rich birnessite

The method of preparation and preliminary characterization of NaBu has been described previously (Drits et al. 1997). Particles were stored in a hydrated state at the synthesized solids concentration (~50 g/L) in polypropylene containers at 5 °C before use.

For the preparation of orientated films of NaBi the following procedure was used. Approximately 5 cm^3 of the NaBu suspension was ultrasonicated for several minutes to ensure good dispersion of the platelets. Then a small quantity of this suspension was deposited within a 2 cm diameter retaining gasket placed on a glass plate. The suspension was allowed to dry slowly in air yielding a solid disk of oriented NaBi. The quantity of suspension deposited within the gasket was calculated to yield a disk of optimum thickness for the X-ray absorption measurements, according to the criterion described in a later section.

Preparation of hexagonal birnessite

All chemical modifications of the NaBu suspensions were conducted at 25 °C with exclusion of light in constant ionic strength (0.1 mol/dm^3 $NaNO_3$) aqueous medium saturated with argon gas. The concentration of solids was approximately 2 g/dm^3. Kinetic studies of the exchange process were conducted in a batch reactor and were initiated in the following way: NaBu was dispersed in the ionic strength medium (typically 10 mL of a 50 g/dm^3 suspension into 250 mL) without adjustment of pH. The pH after dilution was typically in the range 8–9. After an equilibration time of 30 min the pH of the suspension was then rapidly adjusted to, and maintained at, the desired value by addition of a small aliquot of 1.0 mol/dm^3 HNO_3 and then 0.1 mol/dm^3 HNO_3, as controlled by an automatic titration assembly. H^+ additions were recorded directly on a computer. During the course of the reaction the concentration of aqueous Mn and adsorbed Na as well as the average Mn oxidation state were determined using the methods described in the following sections.

Orientated films of HBi were prepared as described for NaBi, except that it was necessary to decant some of the aqueous phase to obtain a suspension of sufficiently high concentration for film preparation.

Aqueous Mn. Aqueous Mn was separated from the solid phase by filtration of 3–5 cm^3 of the suspension through a 0.05 μm pore size filter. Manganese in solution was shown to be exclusively in the form of Mn^{2+} by use of a Mn^{2+}-specific complexing agent (Chiswell et al. 1990). This is the expected result given the very low solubilities of Mn^{3+} and Mn^{4+} in aqueous solutions over the pH range studied (pH 2–5) (Baes and Mesmer 1976). In general the solution concentrations of Mn were determined by either atomic absorption spectroscopy (AAS) or by oxidation to MnO_4^- using potassium periodate (KIO_4) (Kolthoff et al. 1952). In this second method, sam-

ple absorbances were measured at 526 nm and compared to absorbances of known standards (ϵ_{526nm} = 2410 dm³/mol·cm⁻¹).

Structural Na. A 5 cm³ sample of the suspension was collected and centrifuged. The bulk of the aqueous phase was removed and the centrifuge tube then weighed with the remaining concentrated suspension. This suspension was allowed to air dry over several weeks until a constant weight was attained. The dried solid phase was dissolved with 1 cm³ of 10% hydroxylamine hydrochloride ($NH_3OH{\cdot}Cl$) solution and diluted with 1% HNO_3 to a suitable concentration for analysis. Total Mn and Na were measured by inductively coupled plasma (ICP) spectroscopy. Structural Na was calculated as the difference between the total Na measured and that contributed by the included aqueous phase, allowing calculation of the Na^+/Mn ratio in the solid phase.

Average Mn oxidation state. The method used for the measurement of the average oxidation state of Mn in the buserite samples followed that of Freeman and Chapman (1971), except for the measurement of the total Mn content. A mixture of 5.00 cm³ of 0.200 N (0.100 M) sodium oxalate and 2.5 cm³ of concentrated H_2SO_4 was prepared immediately before sampling. A 25 cm³ sample of the buserite suspension (at ~ 2 g/dm³) was added to this mixture. Excess sodium oxalate was titrated with a previously standardized 0.05 N potassium permanganate ($KMnO_4$) solution using an auto-titration system. The determination of the Mn content of the buserite sample was achieved by measurement of the total Mn concentration in the titrated solution with correction for the concentration of Mn added as $KMnO_4$ in the titration procedure. This determination was carried out by oxidation of all Mn to MnO_4^- using the potassium periodate method described above.

Preparation of Zn^{2+}-exchanged birnessite

The Zn^{2+}-exchanged birnessite (ZnBi) sample was prepared by addition of a $Zn(NO_3)_2$ solution to a HBi suspension that had been pre-equilibrated at pH 4. The total Zn concentration after dilution was approximately 5×10^{-3} mol/dm³ and the HBi concentration 2 g/dm³. After allowing several hours for equilibration, the solid was filtered and dried, yielding ZnBi solid.

EXAFS measurements

Mn EXAFS spectra were recorded at the LURE synchrotron radiation laboratory (Orsay, France) on the EXAFS I station. The positron energy of the storage ring DCI was 1.85 GeV and the current between 200 and 300 mA. The incident X-ray beam was monochromatized with a channel-cut Si(331) crystal. X-ray absorption data for Mn were recorded over the energy range 6400–7300 eV, corresponding to a Bragg angle of between 50° and 43°. In this angular range the linear polarization is close to 100% (Hazemann et al. 1992). To avoid sample thickness and heterogeneity effects (Stern and Kim 1981; Manceau and Gates 1997) it was necessary that $\Delta\mu < 1$, where $\Delta\mu$ is the absorption edge step. Homogeneous and flat self-supported films of controlled thickness were prepared for both powder and polarized EXAFS measurements.

Angular measurements were performed in transmission mode by turning film layers around a rotation axis normal to both the beam direction and the electric field vector $\boldsymbol{\epsilon}$. The angular dependence of the EXAFS χ function is given by (Heald and Stern 1977; Brouder 1990): $\chi(\alpha) = [\chi(0°) - \chi(90°)]\cos^2\alpha + \chi(90°)$ where α is the angle between $\boldsymbol{\epsilon}$ and the layer plane. This relationship applies for all photoelectron energies and by means of linear regression and extrapolation, can be used to determine $\chi(90°)$, which cannot be measured experimentally (Manceau et al. 1988, unpublished manuscript). Powder EXAFS spectra were recorded at $\alpha = 35°$ to eliminate any orientation effects (Manceau et al. 1990). X-ray absorption spectra were analyzed according to standard procedures (Teo 1986). A Kaiser function window was used in Fourier transforms to minimize the intensity of side lobes resulting from truncation effects (Manceau and Combes 1988). Manceau (1995) has shown that side lobes associated with the use of a Kaiser window function are of the order of 5% of the intensity of main structural peaks. This low intensity allows greater sensitivity to less pronounced structural features in the RDF and provides strong evidence that peak intensities above this value should be interpreted in structural terms. Interatomic distances and numbers of atomic neighbors were determined using experimental phase shift and amplitude functions derived from suitable reference materials. For Mn-O and Mn-Mn interactions experimental functions were obtained from stoichiometric λ-MnO_2 in which Mn^{4+} atoms are surrounded by six nearest O atoms at 1.91 Å and six nearest Mn atoms at 2.84 Å (Thackeray et al. 1993). For Zn-Mn interactions experimental functions were derived from the phyllomanganate chalcophanite ($ZnMn_3O_7{\cdot}9H_20$) in which Zn^{2+} has six Mn neighbors at an average distance of 3.49 Å (Post and Appleman 1988) (Fig. 11). Through the use of such reference materials it is reasonable to expect an absolute accuracy in the fitted number of neighbors of approximately 10%. The relative accuracy within a series of minerals of similar structures should be better than 10%.

Results

Chemical studies of the NaBu to HBi conversion

Figure 1a shows the kinetic behavior of the adsorbed and solution species involved in the structural alteration of NaBu at pH 4. The reaction is characterized by an initial rapid process in which both Mn^{2+} and part of the Na^+ are released from the solid and exchanged with H^+ from solution. This step is followed by a slower process in which the remaining Na^+ is released and Mn^{2+} (partially) re-adsorbs. The separation of Na^+ desorption into two distinct temporal processes implies that Na^+ occupies at least two types of sites in NaBu. The solid and dashed lines shown for the profiles of Mn^{2+} and H^+, respectively,

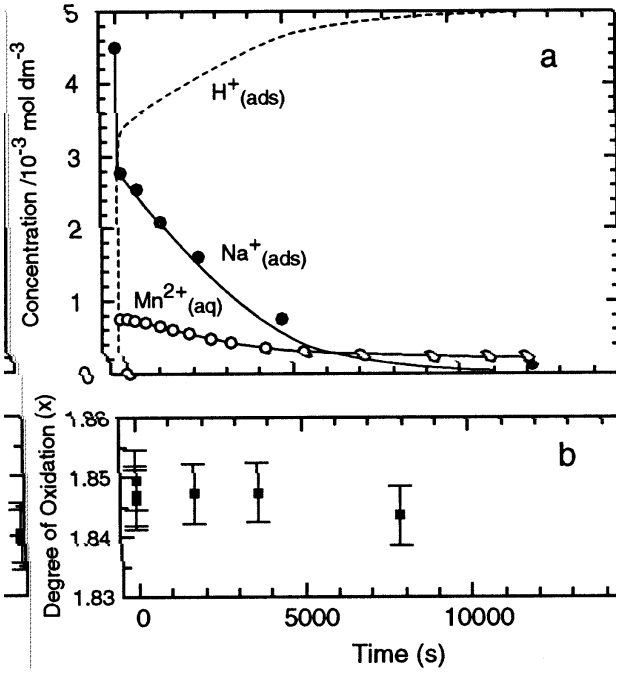

FIGURE 1. (a) Temporal behavior of H^+_{ads} (dashed line), Na^+_{ads} (solid circle), and $Mn^{2+}_{(aq)}$ (open circle) for NaBu undergoing structural alteration at pH 4. The solid line shown for Mn^{2+}_{aq} is an interpolation of the experimental data, whereas the line shown for Na^+_{ads} was calculated on the basis of charge balance considerations, assuming only Na^+, H^+, and Mn^{2+} in the exchange process. Total Mn concentration is 1.54×10^{-2} mol/dm^3. (**b**) Degree of oxidation (x in MnO_x) for NaBu undergoing structural alteration at pH 4.

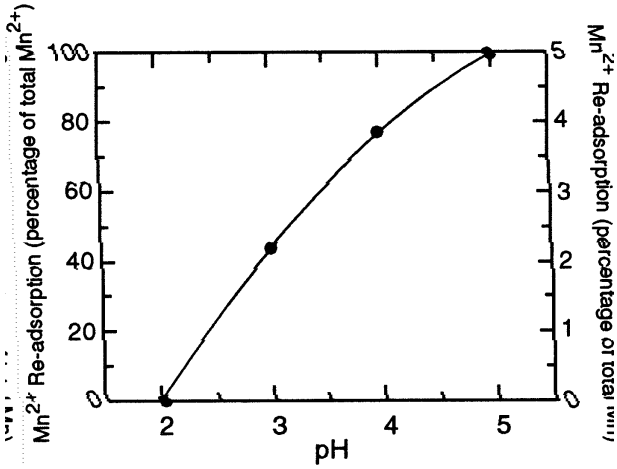

FIGURE 2. Percentage re-adsorption of Mn^{2+}_{aq} at completion of the low pH structural alteration reaction as a function of solution pH.

are interpolations of the experimental data. The solid line shown for Na^+_{ads} was calculated from charge-balance considerations, on the basis that the only cations involved in the exchange process are Na^+, H^+, and Mn^{2+}. Because these are the only cations present in this system, the excellent agreement proves beyond doubt that the aqueous Mn is in the form of Mn^{2+}.

Figure 1b shows the degree of Mn oxidation (x in MnO_x) during the structural alteration reaction. Because the method used for this analysis involved the sampling of the buserite suspension, the values shown are averaged over all Mn in the system, both in the solid and aqueous phases. The measured value does not change during the reaction, which shows that there is no external oxidation of Mn by oxygen under the experimental condition employed. The average of the values shown in Figure 1b corresponds to a degree of oxidation, for the buserite sample used in this study, of $MnO_{1.845 \pm 0.005}$. Previous studies have reported that the low-pH alteration of synthetic NaBu results in the oxidation of the solid phase because of incorporation of O (Giovanoli et al. 1970b). The results of this study do not support such a mechanism. It should be noted however, that the manganese oxide solid does become oxidized during the structural alteration reaction, due entirely to the loss of Mn^{2+} from the solid to the aqueous phase. As shown in the following section, the loss of Mn^{2+} from the solid phase increases with decreasing pH, so under the strongly acidic conditions used by Giovanoli et al. (1970b) in the preparation of their HBi (or $Mn_7O_{13} \cdot 5H_2O$) phase, considerable oxidation of the solid would have been observed. The degree of oxidation is insufficient information for the calculation of the relative proportions of the various Mn oxidation states present in the solid phase. In principle the measured value may correspond to many different combinations of Mn^{4+}, Mn^{3+}, and Mn^{2+}.

The amounts of Na^+ and Mn^{2+} desorbed in the initial rapid reaction were independent of the solution pH over the pH range studied (pH 2–5). The quantity of Mn^{2+} observed in solution corresponds to approximately one-twentieth of the total Mn concentration. The extent of Mn^{2+} re-adsorption as a function of pH is shown in Figure 2. The increased adsorption of Mn^{2+} with increasing pH observed in this system is entirely consistent with previous studies of the adsorption of Mn^{2+} and other hydrolyzable divalent metal ions on manganese oxide colloids (McKenzie 1980). The concentration of Mn^{2+} that appears in solution after the initial rapid process, and that remains in solution at pH < 2, provides a measure of the Mn^{2+} content of the NaBu phase. This Mn^{2+} component, however, could originate from either structural Mn^{2+} in NaBu or as a result of Mn^{3+} disproportionation according to: $Mn^{3+}_{layer} + Mn^{3+}_{layer} \rightarrow Mn^{4+}_{layer} + Mn^{2+}_{aq}$.

These two possibilities for the origin of Mn^{2+} allow the range of possible chemical formulas for NaBu to be calculated. The proportions of Mn^{4+}, Mn^{3+}, and Mn^{2+} in the NaBu phase can be calculated by solving the charge balance and mole balance equations: $4p + 3q + 2r = 2x$ and $p + q + r = 1$, where p, q, and r are the proportions of Mn^{4+}, Mn^{3+}, and Mn^{2+} in the NaBu phase, and x is the degree of oxidation (1.845 for this synthetic NaBu sample). If it is assumed that Mn^{2+} observed in solution

is present in the structure of NaBu, then $r = 0.049$ (one-twentieth of the total Mn), and the chemical formula for NaBu is $Na^{+}_{0.3}Mn^{4+}_{0.739}Mn^{3+}_{0.212}Mn^{2+}_{0.049}O_{\sim 2}$. However, if the Mn^{2+} component is derived from disproportionation of Mn^{3+}, then $r = 0$ and the chemical formula is $Na^{+}_{0.3}Mn^{4+}_{0.69}Mn^{3+}_{0.31}O_{\sim 2}$. It should be noted that in the latter case the Na^{+} and Mn^{3+} contents are almost equal to the maximum values predicted for the type II NaBi microcrystals on the basis of the SAED results of Drits et al. (1997). Given that the Na^{+} to total Mn ratio is quite different in the two types of microcrystals observed for this synthetic NaBu, with approximately 0.2:1 for type I microcrystals and 0.33:1 for type II microcrystals (Drits et al. 1997), the experimentally obtained value would suggest a dominance of type II. This conclusion is consistent with the observations made by Drits et al (1997) in their SAED analysis.

Complete desorption of Na^{+} was observed across the pH range studied (pH 2–5), with the interlayer charge balance maintained by exchange with H^{+} and Mn^{2+}, in varying proportions depending on the solution pH. For this reason, the exchange stoichiometry varies continuously with pH between the limiting cases of:

$$Na^{+}_{ads} + H^{+}_{aq} \rightarrow H^{+}_{ads} + Na^{+}_{aq} \qquad (pH < 2) \qquad (1)$$

and

$$4Na^{+}_{ads} + Mn^{2+}_{aq} + 2H^{+}_{aq} \rightarrow Mn^{2+}_{ads} + 2H^{+}_{ads} + 4Na^{+}_{aq} \qquad (pH > 4) \qquad (2)$$

Given that Na^{+} desorption and Mn^{2+} re-adsorption appear to be independent processes, we ascribe no particular structural significance to the stoichiometry of Equation 2.

Information from EXAFS spectroscopy

Analysis of reference manganese dioxides. The transferability of the phase-shift and amplitude functions derived from λ-MnO_2 was tested on the manganese oxides ramsdellite (γ-MnO_2) (Byström 1949), pyrolusite (β-MnO_2) (de Wolff 1959; Shuey 1975), and romanechite (Turner and Post 1988). Radial distribution functions (RDFs) derived from EXAFS measurements at the Mn *K* edge for these minerals are shown in Figure 3a along with the RDF for λ-MnO_2. The RDF for λ-MnO_2 demonstrates the suitability of this material as a source of phase and amplitude data, with well-isolated peaks at distances, uncorrected for phase shift, of 1.5–1.6 and 2.5 Å corresponding to six O neighbors at 1.91 Å and six Mn neighbors at 2.84 Å, respectively.

The RDFs for the other manganese oxides exhibit prominent peaks at ~1.6, 2.4–2.6, and ~3.1 Å. Given that a nominal correction of 0.3–0.4 Å applies to these distances due phase shift effects, the observed peaks can be assigned to the interactions between Mn-O, Mn-Mn (edge-sharing octahedra), and Mn-Mn (corner-sharing octahedra), respectively (Manceau and Combes 1988). In the case of romanechite the intensity of the Mn-Mn corner-sharing peak is about 20% of the Mn-Mn edge-sharing peak. Based on the previous discussion regarding the size of side lobes associated with the use of a Kaiser window in the Fourier-transform procedure, it is clear that this peak is structural in origin instead of a side lobe of the main Mn-Mn edge-sharing peak.

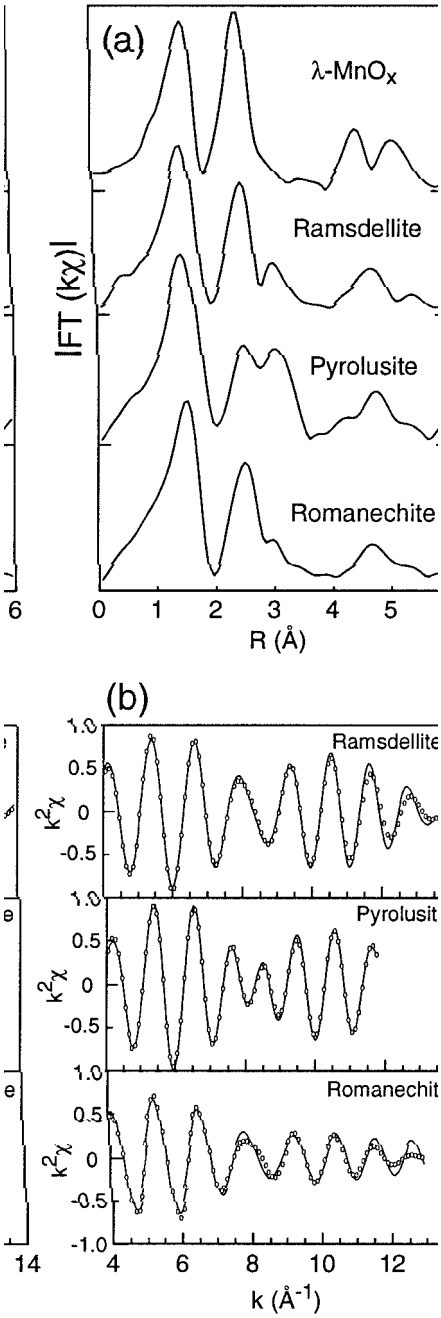

FIGURE 3. (a) Manganese radial distribution functions from EXAFS measurements at the Mn *K* edge for λ-MnO_2, ramsdellite, pyrolusite, and romanechite. (**b**) Fourier-filtered $\chi_{Mn\text{-}Mn}$ contributions to EXAFS spectra (solid lines) with fits (open circles) for ramsdellite, pyrolusite, and romanechite. Fitted parameters are given in Table 1.

TABLE 1. Mn-O and Mn-Mn distances and amplitudes (number of neighbors) for reference Mn oxides, as determined from EXAFS data

	Mn-O				Mn-Mn_1 (Edge linkage)			Mn-Mn_2 (Corner linkage)			
Reference Material	R_{Mn-O} (Å)	$\Delta\sigma$ (Å)	$N_{(O)}$	ΔE (eV)	R_{Mn-Mn} (Å)	$\Delta\sigma$ (Å)	N_{Mn_1}	R_{Mn-Mn} (Å)	$\Delta\sigma$ (Å)	N_{Mn_2}	Mn-Mn ΔE(eV)
Ramsdellite	1.90	0.00	4.8	0.6	2.86	0.01	3.7	3.42	0.02	4.0	2.6
	(1.89)		(6.0)		(2.89)		(4.0)	(3.43)		(4.0)	
Pyrolusite	1.89	0.01	5.5	1.3	2.86	0.00	2.0	3.42	0.03	7.8	3.3
	(1.88)		(6.0)		(2.87)		(2.0)	(3.43)		(8.0)	
Romanechite	1.91	0.01	4.2	2.1	2.87	0.04	4.6	3.46	0.04	3.4	2.6
	(1.93)		(6.0)		(2.90)		(4.4)	(3.43)		(3.2)	

Note: Mn-O and Mn-Mn distances and amplitudes were fitted with experimental phase-shift and amplitude functions extracted from λ-MnO_2 (Thackeray et al. 1993). Values in brackets are the interatomic distances and number of neighbors as determined from XRD data for ramsdellite (Byström 1949), pyrolusite (de Wolff 1959), and romanechite (Turner and Post 1988). ΔE values correspond to the shift of the *K*-edge energy threshold.

Good fits of the Fourier-filtered Mn-O contributions to the EXAFS spectra were obtained for all three manganese oxides. Fitted values of R_{Mn-O} and the number of neighbors (N_O) are shown in Table 1. N_O values obtained are slightly lower than those determined by X-ray diffraction because of the higher degree of disorder in Mn-O distances in these materials compared to the reference λ-MnO_2 material. In the case of romanechite the fitted ΔE value is slightly higher and probably reflects the greater distribution of Mn-O distances in this sample in comparison with the other reference manganese dioxides. First and second Mn-Mn contributions were fitted together because of incomplete separation in the Fourier-filtering process. The fits to these spectra for the three test minerals are shown in Figure 3b and the fit parameters given in Table 1. Good agreement is obtained for Mn-Mn distances and the number of neighbors for all manganese dioxide materials examined. Again romanechite shows some anomalous behavior with rather large $\Delta\sigma$ values required to achieve a good fit to the data. This can probably be attributed to a wider distribution of Mn-Mn distances because of the presence of some lower valence Mn in this mineral (Wadsley 1953; Turner and Post 1988). Quite clearly, the amplitude and phase-shift functions extracted from λ-MnO_2 lead to fitted EXAFS parameters for these reference manganese oxides, which are in good agreement with the crystallographically determined values. For this reason we can be confident that these same amplitude and phase-shift functions are suitable for the analysis of the EXAFS spectra of the synthetic birnessite samples prepared in this study.

Powder EXAFS data for NaBi and Hbi: Qualitative results. Figure 4 shows the Mn RDFs for NaBi at pH 9 and several HBi phases equilibrated at constant pH, between pH 5–2. Also shown in this figure are the Mn and Zn RDFs for chalcophanite and the Zn RDF for ZnBi.

Apart from the first peak corresponding to Mn-O interactions, the RDF of NaBi exhibits one strong cation-cation peak at the uncorrected distance of 2.5–2.6 Å. Again assuming a phase-shift correction of 0.3–0.4 Å, this peak corresponds to a structural distance of 2.8–2.9 Å, which is a typical distance for edge-sharing MnO_6 octahedra and similar to the values found for the manganese oxide reference minerals described previously. The absence of a peak at 3.1 Å indicates that there are no detectable corner-sharing octahedra in NaBi and that the Mn octahedra are almost exclusively edge-linked. Similar conclusions were made by Strobel et al. (1987), Manceau et al. (1992), and Post and Veblen (1990). The only other major peaks in this spectrum are those corresponding to the second sphere of cations in the layer, in the range 4.7–5.1 Å.

The Mn RDFs for the HBi samples are all similar and distinctly different from that for NaBi. In particular there is a peak at 3.1 Å in addition to the main Mn-Mn peak at 2.5 Å. This peak corresponds to a structural distance of 3.4–3.5 Å and therefore to corner-sharing MnO_6 octahedra. The minimum intensity for this peak is observed for the pH 2 sample, but even in this case the intensity of the peak is 10% of the intensity of the Mn-Mn edge-sharing peak. When compared to the expected intensity of side lobes resulting from the Kaiser window function used in the Fourier-transform procedure of 5%, it is clear that in all HBi samples the 3.1 Å peak is structural in nature. Further confirmation of the structural nature of this peak is the absence of a similar peak in the Mn RDF of NaBi. Because all spectra were treated in exactly the same way, if this peak were a side lobe originating from truncation effects of the window function used, it would appear in all spectra. Two strong peaks are observed at longer distances (4.7 and 5.2 Å) in the HBi Mn RDFs. As for NaBi these peaks correspond to second and third Mn neighbors in the layers, although for the HBi samples the intensities of these peaks are considerably greater.

The Mn RDF for chalcophanite shows a strong similarity to the Mn RDF for the HBi samples, suggesting a similarity in the structure of these materials, as suggested previously (Giovanoli et al. 1970b). At the Zn *K* edge for chalcophanite the peak corresponding to the corner-sharing distance (3.2 Å uncorrected) is considerably enhanced because Zn is exclusively located on lattice vacancy sites in this mineral with six nearest neighbor Mn atoms at the crystallographic distance of 3.49 Å (Wadsley 1955; Post and Appleman 1988). The Zn RDF of ZnBi shows strong

FIGURE 5. Fourier-filtered $\chi_{Mn\text{-}Mn}$ contributions to Mn EXAFS spectra of NaBi (pH 9) and HBi (pH 2–5). Solid lines are experimental spectra whereas the open circles are fits. The first pair of spectra in this figure show a comparison of the Fourier-filtered $\chi_{Mn\text{-}Mn}$ contribution for λ-MnO_2 (solid line) with that for NaBi (dotted line), demonstrating the considerable differences in amplitude envelopes for these samples. Fitted parameters are given in Table 2.

→

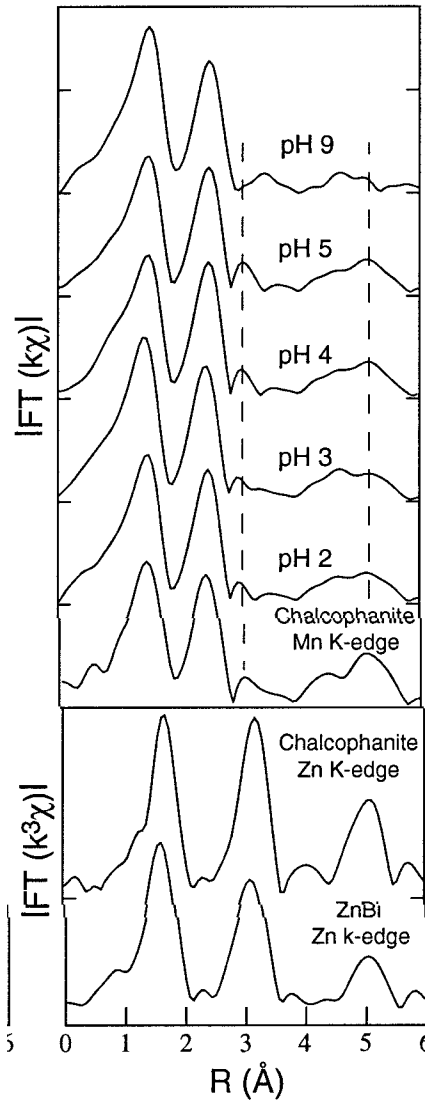

FIGURE 4. Manganese radial distribution functions from EXAFS measurements at the Mn *K* edge for NaBi (pH 9), HBi (pH 2–5), and chalcophanite, and the Zn radial distribution function from EXAFS measurements at the Zn *K* edge for chalcophanite and ZnBi.

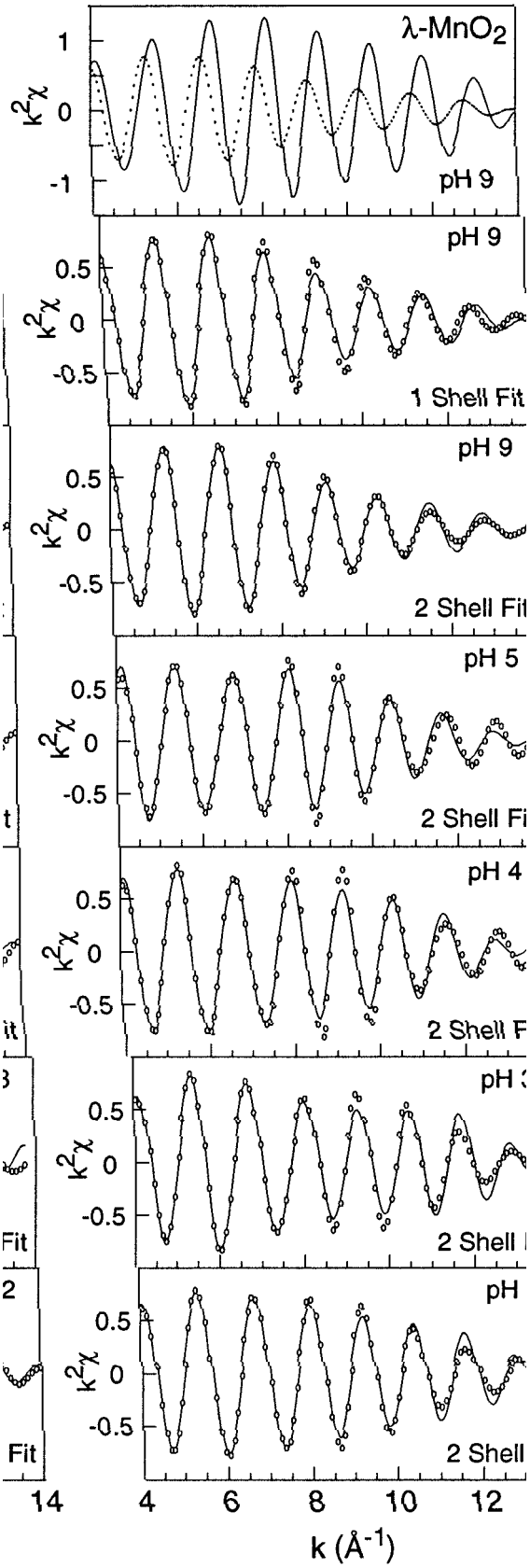

TABLE 2. EXAFS parameters for Mn-Mn pairs in NaBi and HBi and the Zn-Mn pair in ZnBi

	Mn-Mn_1			Me-Mn_2				Mn-$Mn_{1\frac{1}{4}}$			
Sample	$R_{Mn\text{-}Mn_1}$ (Å)	$\Delta\sigma$ (Å)	N_{Mn}	$R_{Me\text{-}Mn_2}$ (Å)	$\Delta\sigma$ (Å)	N_{Mn}	Me-$Mn_{1\frac{1}{2}}$ ΔE(eV)	$R_{Mn\text{-}Mn_3}$ (Å)	$\Delta\sigma$ (Å)	N_{Mn}	ΔE (eV)
NaBi pH9	2.88	0.0	3.9	3.02	0.01	2.9	−1.2				
HBi pH5	2.87	0.01	4.1	3.52	0.03	2.0	−1.0				
HBi pH4	2.87	0.01	4.1	3.49	0.03	2.0	1.6	5.01	0.02	5*	0.8
								5.61	0.02	16*	0.8
HBi pH3	2.86	0.01	4.3	3.47	0.02	2.0	2.0				
HBi pH2	2.87	0.01	4.6	3.47	0.03	1.7	1.6				
ZnBi				3.45	0.01	5.8	2.5				

* Values unreliable due to multiple scattering effects.

similarity to the Zn RDF of chalcophanite, although the corner-sharing peak occurs at a slightly shorter distance. This observation strongly suggests that Zn^{2+} occupies similar structural positions in these two materials. The Zn RDF for chalcophanite also shows an atomic neighbor at 4.1 Å, corresponding to Zn-Zn interactions between the pairs of Zn^{2+} cations across lattice vacancy sites, i.e., above and below vacancy sites. It is interesting to note that this peak is absent in the Zn RDF of ZnBi.

Quantitative analysis. Figure 5 shows fits to Fourier-filtered Mn-Mn interactions for the NaBi and HBi samples. Also shown is a comparison of the Fourier-filtered Mn-Mn edge-sharing interaction for the reference λ-MnO_2 material with that for NaBi (first pair of spectra in Fig. 5). Fitting parameters and best-fit values for the number of neighbors and distances for the synthetic birnessite samples are given in Table 2. The second spectrum in Figure 5 shows the Fourier-filtered EXAFS spectrum of the Mn-Mn edge-sharing distance in NaBi (solid line) along with a one-shell fit to this spectrum. The assumption of a single structural distance provides an approximate fit to this spectrum. The amplitude mismatch in the range 9–11 $Å^{-1}$ and the phase mismatch at higher k values, however, suggest the presence of at least one other Mn-Mn distance. Support for this conclusion is provided by the comparison of the NaBi spectrum with the spectrum of λ-MnO_2, demonstrating the considerable differences in the shapes of the amplitude envelopes for these two samples. A two-shell fit to the NaBi EXAFS data (third spectrum) yields good agreement over the entire k range, corresponding to distances of 2.88 ± 0.05 Å (N_{Mn} = 3.9) and 3.02 ± 0.05 Å (N_{Mn} = 2.9). Assuming a dominance of type II microcrystals [on the basis of the chemically derived Na^+ to total Mn ratio and the SAED observations (Drits et al. 1997)], in which every third row of Mn octahedra running in the [010] direction contains dominantly Mn^{3+}, the expected Mn-Mn distances and amplitudes can be estimated. Figure 6a shows the expected Mn-Mn distances in the layers of NaBi, calculated on the basis of both the a and b parameters reported previously (Drits et al. 1997) and the charge distribution in the layers. Mn^{4+}-Mn^{4+} and Mn^{3+}-Mn^{3+} distances in the [010] direction equal the b parameter value of 2.847 Å with N_{Mn} = 2.0. The Mn-Mn distances in the (110,1$\bar{1}$0) directions are longer because of the elongation of the Mn^{3+} octahedra. As expected, the longest Mn-Mn distances in these directions occur between Mn^{4+}-Mn^{3+} pairs because of the localization of layer distortion on the Mn^{3+} rich rows. Mn^{4+}-Mn^{4+} distances in the (110,1$\bar{1}$0) directions, however, also increase because of the migration of Mn^{4+} cations toward the Mn^{3+} rich rows, as a result of the incomplete charge compensation of the shared O atoms. We estimate that Mn-Mn distances in these directions vary periodically between ~3.00 Å for Mn^{4+}-Mn^{3+} pairs and ~2.90 Å for Mn^{4+}-Mn^{4+} pairs with N_{Mn} = 2.7 and N_{Mn} = 1.3, respectively. The two-shell fit to the Fourier-filtered Mn-Mn EXAFS spectrum of NaBi can be understood if it is assumed that all Mn-Mn pairs in the [010] direction and Mn^{4+}-Mn^{4+} pairs in the (110,1$\bar{1}$0) directions are fitted as one shell with an average distance of ~2.87 Å (N_{Mn} = 3.3) and Mn^{4+}-Mn^{3+} pairs in the (110,1$\bar{1}$0) directions are fitted as a longer distance shell at ~ 3.00 Å (N_{Mn} = 2.7). These values compare well with the experimental EXAFS results of N_{Mn} = 3.9 at 2.88 Å and N_{Mn} = 2.9 at 3.02 Å. Of course it would be structurally more accurate to fit the NaBi edge-sharing peak as a three-shell system. Unfortunately, because of the limited reciprocal space of EXAFS spectra (14 $Å^{-1}$) it is not possible to resolve distances that are separated by less than ~0.12 Å. In general, however, the EXAFS results support the structural model developed by Drits et al. (1997) for the layers of NaBi. As discussed by Drits et al. (1997), very few lattice vacancies in the NaBi sample exist, which means that the total number of neighbors should be close to six. The EXAFS-derived value of 6.8 ± 0.7 is consistent with the absence of vacancies in the layers of NaBi.

For all the HBi samples it was necessary to fit both the edge-sharing and corner-sharing peaks, at 2.5 Å and 3.1 Å, respectively, together because of the incomplete separation of these two peaks in the Fourier-filtering process. The Fourier-filtered EXAFS spectra shown in Figure 5 for the HBi samples (both peaks combined) therefore display a wave beating in the range 6–10 $Å^{-1}$, which can be related to the expected difference in shell distances of $0.5 \leq \Delta R[= (3\pi/2k)] \leq 0.8$. Reasonable two-shell fits are obtained across the entire k range for all spectra. For all the HBi samples the Mn-Mn edge-sharing distance is 2.87 ± 0.02 Å, a distance that is shorter than that observed

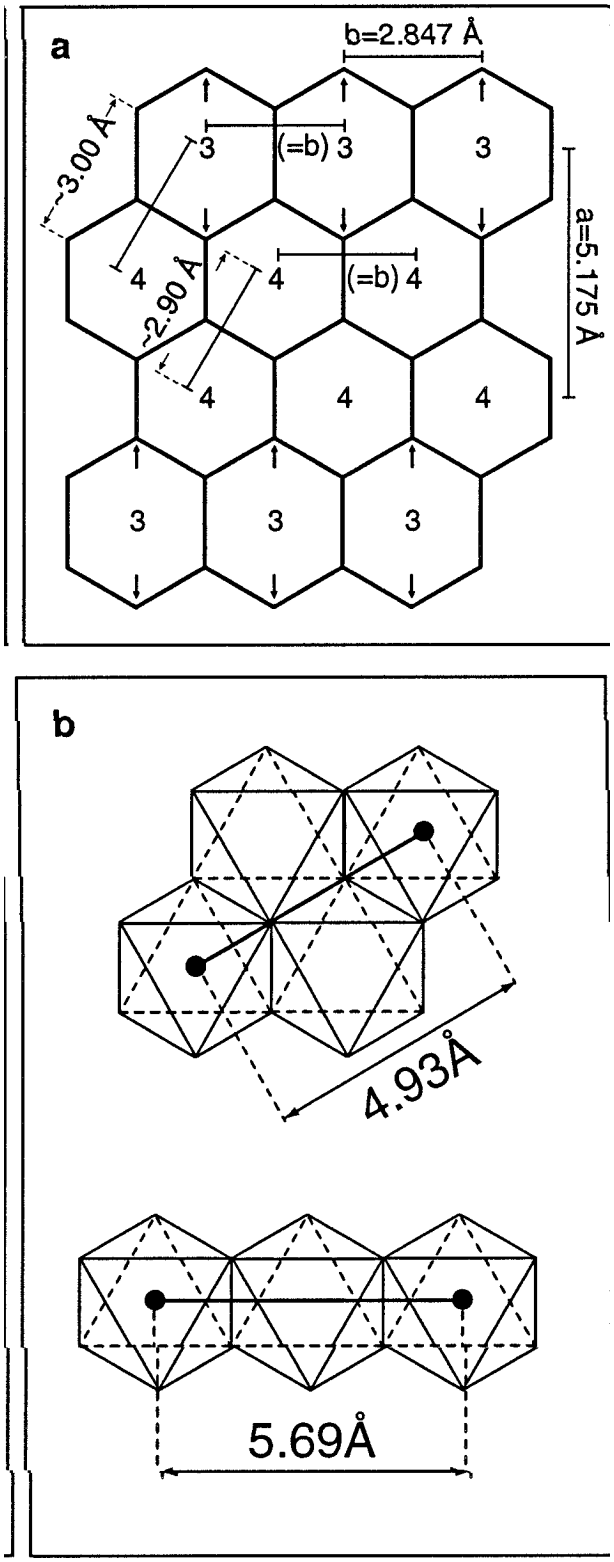

FIGURE 6. **(a)** A structural diagram showing the ordering of Mn^{4+} and Mn^{3+} octahedra in the layers of NaBi (type II microcrystals). Mn-Mn distances in this figure were calculated on the basis of both the *a* and *b* parameters reported by Drits et al. (1997), taking into account the charge distribution in the layers. (**b**) **Top** shows Mn-Mn neighbors along an edge for HBi microcrystals, corresponding to a distance of 5.0 Å (from EXAFS measurements) or 4.93 Å (from SAED and XRD measurements), see Drits et al. (1997). (**b**) **Bottom** shows Mn-Mn neighbors across two edges for HBi microcrystals, corresponding to a distance of 5.6 Å (from EXAFS measurements) or 5.69 Å [from SAED and XRD measurements, see Drits et al. (1997)].
←

for NaBi, taking into account that two Mn-Mn edge-sharing distances are found for NaBi (2.88 and 3.02 Å). This would suggest a decrease in the lower valence Mn content of the layers in HBi. The second fitted distance, in the range 3.47–3.52 Å, is similar to that found for the Fourier-filtered Zn-Mn distance in ZnBi of 3.45 ± 0.05 Å (see Table 2) and a range of values that compare closely with that for chalcophanite at 3.49 Å (Post and Appleman 1988). Based on the similarity of the ionic radii of Zn^{2+} (R_{Zn} = 0.74 Å) and of Mn^{2+} ($R_{Mn^{2+}}$ = 0.83 Å) and Mn^{3+} ($R_{Mn^{3+}}$ = 0.65 Å), this would strongly support a structural similarity within this group of minerals. For this reason we propose that the corner-sharing Mn-Mn distance observed in the HBi EXAFS spectra corresponds to Mn adsorbed on vacancy sites, that is, triple corner (TC) sharing Mn. The fitted TC-sharing distances for the HBi series increase with increasing pH from 3.47 Å at pH 2 to 3.52 Å at pH 5. This trend agrees with the qualitative interpretations of the RDFs for these samples (Fig. 4). Assuming that the TC-sharing distance is directly related to the radius of the cation adsorbed at lattice vacancies, and keeping in mind the ionic radii values given above for Mn^{3+}, Mn^{2+}, and Zn^{2+}, the observed TC-sharing distances suggest that there is a mixture of Mn^{2+} and Mn^{3+} at vacancy sites in HBi. As shown later in this article, this assignment of the Mn valency at vacancies is strongly supported by polarized EXAFS studies.

In the RDFs shown in Figure 4 for the HBi series of samples, the intensity of the TC-sharing peak increases with increasing pH. In general terms this trend is supported by the EXAFS data in Table 2 for these samples, which show the TC-sharing amplitude changing from N_{TC} = 1.7 at pH 2 to N_{TC} = 2.0 at pH 5. However, the fitted number of TC-sharing neighbors for these samples does not increase in an orderly way with increasing pH and therefore cannot be interpreted as unequivocal proof of a structural trend in the HBi series. Additional support for this interpretation is provided by the corresponding number of edge-sharing neighbors, which steadily decreases with increasing pH from N_E = 4.6 at pH 2 to N_E = 4.1 at pH 5. Because the EXAFS method provides an average of the local structures of all Mn atoms in the sample, a decrease in the number of edge-sharing neighbors must be accompanied by an increase in the number of TC-shar-

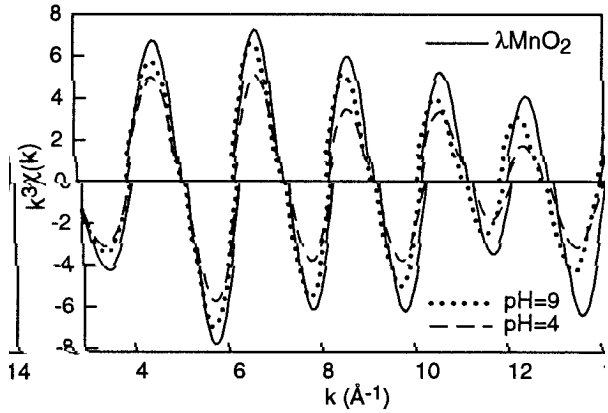

FIGURE 7. Fourier-filtered $\chi_{Mn\text{-}O}$ contributions to Mn EXAFS spectra of λ-MnO_2, NaBi (pH 9), and HBi (pH4). These spectra clearly show the smaller amplitude of the EXAFS oscillations for the birnessite samples compared to the reference λ-MnO_2 material.

ing neighbors. The fact that the expected trend in the number of TC-sharing neighbors is poorly reflected in the fitted EXAFS parameters is most likely due to the small contribution that the TC-sharing peak makes to the Fourier-filtered EXAFS spectrum. The increase in the number of TC-sharing neighbors with increasing pH, combined with the observed increase in the re-adsorption of Mn^{2+} with increasing pH (Fig. 2), suggests that the re-adsorption of Mn^{2+} on HBi occurs at lattice vacancies. This behavioral trend also explains the increase in TC-sharing distance with increasing pH for the HBi series of samples.

As noted previously there is a significant difference in the amplitude of the peaks in the range 4.7–5.2 Å for the NaBi and HBi samples. Comparison with the number of edge-sharing neighbors for these samples shows that this difference in intensity cannot be correlated with the expected number of neighbors at these longer distances. The two peaks in this range were fitted as a two-shell system for the pH 4 HBi sample (spectra not shown) with the best-fit values given in Table 2. The amplitude was poorly reproduced over the *k* range, however the frequency was well matched indicating that the fitted distances were reliable. The fitted number of neighbors for these Fourier-fitted peaks is therefore not accurate. The two distances of 5.0 and 5.6 Å can be related to second-neighbor Mn-Mn distances along edges [Fig. 6b(top)] and across two edges of the phyllomanganate layer [Fig. 6b(bottom)]. These values compare with the values of 4.93 and 5.69 Å, respectively, calculated from the unit-cell parameters for HBi (Drits et al. 1997). The high intensity of the second of these peaks (across two edges), despite the long distances involved, is striking and can be attributed to the so called ''focusing effect,'' which is commonly observed in layered metal oxides and hydroxides (O'day et al. 1994). The focusing effect is a result of multiple scattering (MS) of the ejected photoelectron and results in a substantial increase in the EXAFS amplitude. The simulation of MS spectra is beyond the scope of this paper, but it suffices to say that typically MS effects are observed for layered structures where there is strong linear alignment of layer cations and little variation in the cation-cation distances. Drits et al. (1997) noted that a principal difference between NaBi and HBi is the change from a distorted hexagonal symmetry to an undistorted hexagonal symmetry of layers. In the case of NaBi it is clear that there is considerable variation in the Mn-Mn distances, especially in the [110] and [1$\bar{1}$0] directions where the cation sequence is Mn^{4+}-Mn^{3+}-Mn^{4+}. This incoherence in the cation-cation distances of NaBi explains the low intensity of the RDF signal of NaBi in the 4–5 Å range (Fig. 4). The EXAFS results allow us to conclude that there are significantly fewer Mn^{3+} centers in the layers of HBi than NaBi.

TABLE 3. EXAFS parameters for Mn-O pairs in NaBi and HBi

	Mn-O			
Sample	$R_{Mn\text{-}O}$ (Å)	Δσ (Å)	N_O	ΔE (eV)
NaBi pH9	1.92	0.01	5.5	1.0
HBi pH5	1.90	0.01	4.5	1.0
HBi pH4	1.91	0.01	4.7	1.0
HBi pH3	1.91	0.01	5.2	1.0
HBi pH2	1.91	0.01	4.9	1.5

Figure 7 shows Fourier-filtered Mn-O EXAFS spectra for λ-MnO_2, NaBi, and HBi (pH 4). The amplitude of the EXAFS oscillations decreases in the order λ-MnO_2 > NaBi > HBi suggesting a corresponding trend in the number of O neighbors or a greater disorder in the Mn-O distances. Good fits were obtained for the Fourier-filtered Mn-O EXAFS contributions for all synthetic birnessite samples by assuming a single atomic shell (Table 3). Consistent with the EXAFS spectra shown in Figure 7, the Mn-O pair for NaBi is fitted to a slightly longer average distance and a higher amplitude than for the HBi samples. The difference in Mn-O distances can be partly attributed to the loss of some Mn^{2+} from the solid, i.e., to the decrease in Mn^{2+} re-adsorption at decreasing pH. The decrease in amplitude upon conversion of NaBi to HBi can be correlated with an increase of TC-sharing Mn in the HBi samples. Mn adsorbed in this way is coordinated to three O atoms of the layer and three H_2O molecules, as for Zn^{2+} in chalcophanite. The disorder in the $Mn_{interlayer}$-O octahedra is high, due to the presence of both Mn-O and Mn-OH_2 bonds, resulting in a broader distribution of Mn-O distances for these Mn cations. For example, in chalcophanite the Zn-O and Zn-OH_2 distances were measured as 2.07 and 2.14 Å, respectively (Post and Appleman 1988). This disorder results in a lower back-scattering amplitude, as observed in the experimental data.

Polarized EXAFS Spectra of NaBi and HBi. In polarized EXAFS measurements, the amplitude of the EXAFS contribution for each atomic pair depends on its angle with respect to the electric field vector **ϵ**. This angular

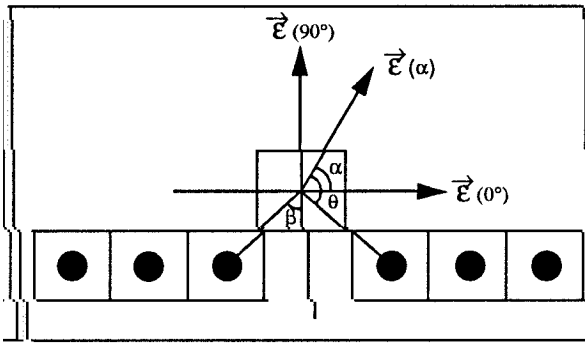

FIGURE 8. Schematic diagram of the relative orientation of a birnessite layer to the electric field vector ($\boldsymbol{\epsilon}$). The angle between the layer and the electric vector is denoted α; β is the angle between the vector connecting the atomic pair of interest and the perpendicular to the layer, and θ is the angle between the vector connecting the atomic pair of interest and the electric field vector.

dependence can be written (Teo and Lee 1979; Stern and Heald 1983):

$$\chi(k, \theta) = \sum_j \sum_{i=1}^{N_j} 3 \cos^2(\theta_i^j)\chi_{iso}^j(k) \qquad (3)$$

where the index j is over all atomic shells around the absorbing atom, the index i is over all N_j atoms of the jth shell, θ_i^j is the angle between the polarization vector $\boldsymbol{\epsilon}$ and the vector $\mathbf{r}_i^j$ that connects the absorbing atom to the ith atom of the jth shell and χ_{iso} is the EXAFS amplitude for the powder spectrum. Equation 3 shows that when $\boldsymbol{\epsilon}$ is pointed toward a given backscatterer, the EXAFS amplitude is enhanced by a factor of three. As a result of this property, angular measurements provide information of both a direction-dependent structural and chemical nature and allow the detection of weak atomic shell contributions that otherwise are undetectable in the analysis of powder spectra.

Manceau et al. (1990) demonstrated that the variation of the EXAFS amplitude $\chi(k,\theta)$ with the angle between $\boldsymbol{\epsilon}$ and the layer (α) depends on the angle between the vector connecting the atomic pair of interest and the perpendicular to the layer (β) (see Fig. 8). For β = 54.7°, $3\cos^2\theta_j$ is equal to one and the EXAFS amplitude is independent of the orientation angle (α) [$\chi(k,\theta) = \chi_{iso}(k)_j$] effectively forming a magic angle for the mineral phase. For $\beta < 54.7°$ $\chi(k,\theta)$ increases with increasing values of α, while for $\beta > 54.7°$ $\chi(k,\theta)$ decreases with increasing α.

For cations adsorbed at layer vacancy sites, it is logical to conclude that smaller cations are closer to the Mn layer and hence have a larger β angle. The series of cations, in order of increasing ionic radius, Mn^{4+} (0.53 Å), Mn^{3+} (0.65 Å), Zn^{2+} (0.74 Å), and Mn^{2+} (0.83 Å), should therefore exhibit decreasing β angles when adsorbed on lattice vacancy sites. The mineral chalcophanite provides a suitable reference point for the assessment of the polarized EXAFS spectra of NaBi and HBi. In chalcophanite the vector connecting Zn^{2+} and the nearest Mn cations in the layer form a β angle of 53.5°, very close to the magic-angle value. Accordingly the intensity of the Zn-Mn TC-sharing peak in the RDF of chalcophanite is independent of orientation angle. Based on the relative ionic radii for Zn^{2+} and Mn cations it is reasonable to expect that for synthetic birnessite samples with Mn^{3+} or Mn^{4+} adsorbed at lattice vacancy sites the β angle would be greater than or 54.7° resulting in a decreasing intensity for the Mn-Mn TC-sharing peak with increasing orientation angle. For synthetic birnessite samples with Mn^{2+} adsorbed at vacancy sites, the opposite behavior should be observed.

Figures 9a and 9b show polarized EXAFS spectra of

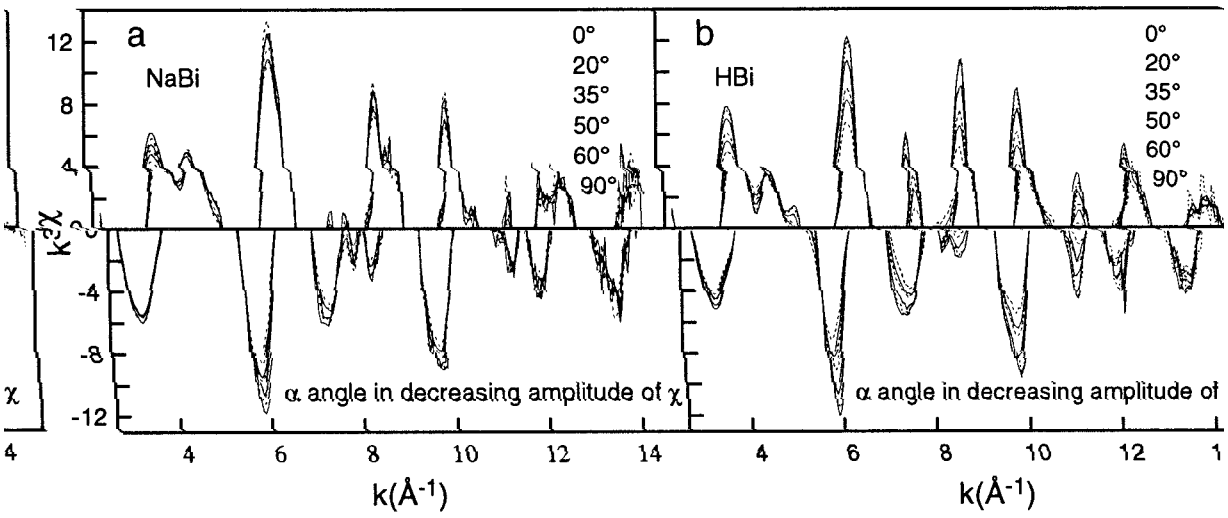

FIGURE 9. Polarized EXAFS spectra recorded at the Mn *K* edge for (**a**) NaBi and (**b**) HBi at α 0°, 20°, 35°, 50°, and 60°. The 90° spectra were calculated using the method described in the experimental section.

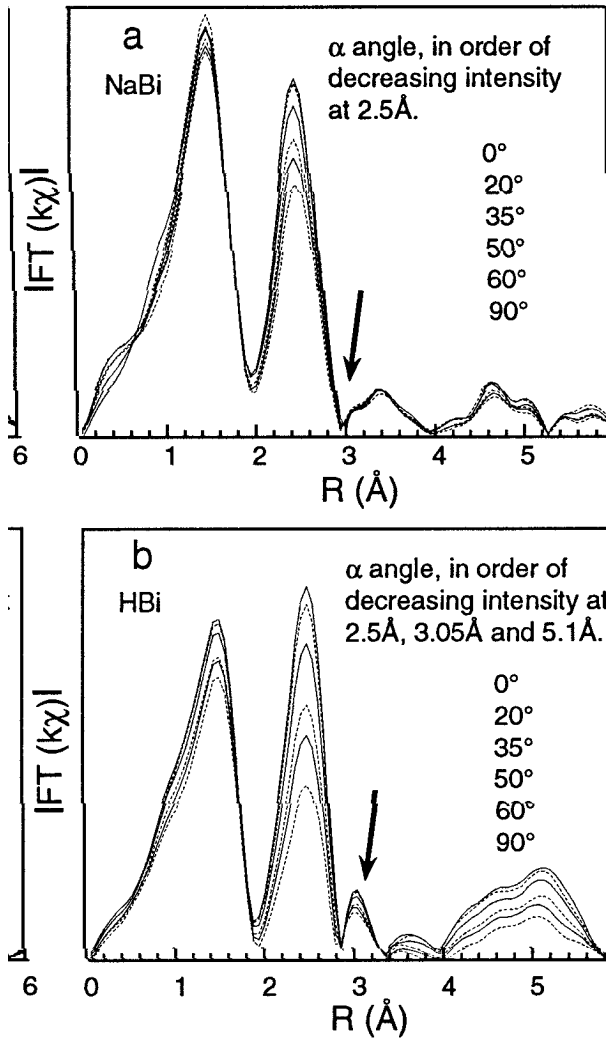

FIGURE 10. (a) Mn RDFs for NaBi, derived from the Mn EXAFS spectra shown in Figure 9a. (**b**) Mn RDFs for HBi, derived from the manganese EXAFS spectra shown in Figure 9b.

NaBi and HBi (pH 4), respectively. Of particular importance in these spectra is the presence of isosbestic points at which $\chi(k)$ is independent of α. The presence of these points indicates a high homogeneity in the sample thickness and provides good evidence that the differences between these spectra are due to orientation effects alone. Accordingly the observed changes in amplitude can safely be interpreted in terms of structural properties. The 90° spectra shown in these figures were calculated using the linear regression method described in the experimental section. Figures 10a and 10b show the RDFs corresponding to the EXAFS spectra shown in Figures 9a and 9b, respectively. Perfect orientation of the synthetic birnessite layers should result in a 90° spectrum in which there is no contribution from Mn-Mn edge-sharing interaction because under these conditions the electric field vector and the layer are orthogonal. In both sets of RDFs there is a contribution because of Mn-Mn edge-sharing octahedra in the 90° spectra; this is more pronounced for the pH 9 spectrum. The unexpected presence of this peak in both samples indicates that perfect orientation of the synthetic birnessite microcrystals was not achieved. Despite this limitation it is clear that the microcrystals are highly orientated, thus allowing analysis of the spectra in terms of structural effects. A particular feature to note from the set of spectra at pH 9 is the absence of significant intensity at 3.1 Å (indicated by the arrow, Figs. 10a and 10b) at all angles. The structural results of Drits et al. (1997) show that if any TC-sharing Mn exists in NaBi, it can only occur in the form of Mn^{2+}, resulting from disproportionation along Mn^{3+}-rich rows. Because the ionic radius of Mn^{2+} is greater than that of Zn^{2+}, the β angle formed by Mn^{2+} adsorbed on lattice vacancies is less than 54.7°. For this reason, any Mn-Mn TC-sharing interactions in NaBi should be maximized in the 90° RDF. The absence of the 3.1 Å peak in the 90° RDF allows us to conclude that there can only be very little, if any, TC-sharing Mn in NaBi. Clearly, any interlayer Mn^{2+} in NaBi does not sorb above or below lattice vacancy sites and must therefore occupy other specific interlayer sites.

Of great interest in the polarized RDFs for HBi (Fig. 10b) is the behavior of the Mn-Mn TC-sharing peak at 3.05 Å. It is clear that the intensity of this peak decreases with orientation angle, leading to the direct conclusion that the β angle is greater than 54.7°. Keeping in mind the order of increasing ionic radius $Mn^{4+} < Mn^{3+} < Zn^{2+} < Mn^{2+}$ and the β angle in chalcophanite of 53.5°, it can be concluded that the ionic radius of Mn cations located at vacancy sites in HBi is, on average, smaller than that of Zn^{2+}. The majority of Mn cations at these sites at pH 4 must therefore be Mn^{3+} or Mn^{4+} rather than Mn^{2+}.

The absence of any detectable peak at 4.0 Å in the polarized EXAFS spectra of HBi at all angles shows that there are unlikely to be any pairs of Mn cations across lattice vacancy sites. It is important, however, to be cautious in this interpretation. In the chalcophanite Zn RDF (Fig. 4) the peak corresponding to Zn-Zn interactions across vacancy sites is quite strong because Zn^{2+} is located exclusively on vacancy sites, and all Zn^{2+} atoms have a neighbor at the crystallographic distance of 4.25 Å. For EXAFS spectra recorded at the Mn *K* edge for HBi, the intensity of any Mn-Mn across-vacancy interactions will be diminished significantly because of the averaging of local Mn environments in the sample. For this reason we must be less definite about the absence of Mn-Mn pairs across lattice vacancy sites.

DISCUSSION

Structure of NaBi

The structures of synthetic NaBi and NaBu have been likened to that of chalcophanite by several authors (Giovanoli et al. 1970a; Burns and Burns 1977; Post and Veblen 1990; Manceau et al. 1992). On the basis of the results presented by Drits et al. (1997) and in this paper, this analogy can be considerably refined. NaBi is a layered man-

ganese oxide formed by edge-sharing MnO_6 octahedra and in this sense is similar to chalcophanite. In the chalcophanite layers one in every seven cation sites is vacant, with Zn^{2+} ions coordinated above and below these sites (Wadsley 1955; Post and Appleman 1988). NaBi differs considerably, with no evidence for significant numbers of layer vacancies or corner-sharing Mn octahedra. The results of the polarized EXAFS measurements provide strong confirmation of this last point. NaBi and chalcophanite must therefore have considerably different interlayer structures. In chalcophanite the mechanism of layer-layer stabilization is the hydrogen bonding between TC-sharing Zn^{2+} ions and adjacent layers. Layer-layer stabilization in NaBi must occur by means of the strong association of Na^+ with the excess negative charge in the layers, combined with some degree of hydrogen bonding between layer O atoms and interlayer H_2O molecules. Both the absence of layer vacancies and the high proportion of layer Mn^{3+} in NaBi are consistent with the Rietveld refinement of synthetic NaBi by Post and Veblen (1990). In particular the Mn site-occupancy factor was found by these authors to be close to 1.0 (indicating very few vacancies) and the mean Mn-O distance was equal to that expected for a layer with 75% Mn^{4+} and 25% Mn^{3+}. These values are of course approximate but lie within the range of chemical formulae for NaBu and NaBi presented earlier, between $Na^+_{0.3}Mn^{4+}_{0.739}Mn^{3+}_{0.212}Mn^{2+}_{0.049}O_{\sim 2}$ and $Na^+_{0.3}Mn^{4+}_{0.69}Mn^{3+}_{0.31}O_{\sim 2}$, corresponding to the possible presence or absence of Mn^{2+}, respectively, in NaBu and NaBi.

The XRD data of Kuma et al. (1994) showed that the conversion of synthetic NaBu to NaBi is characterized by a reduction of the *a* parameter, which on the basis of the conclusions drawn by Drits et al. (1997) shows a decrease in the Mn^{3+} content of the layers. As was discussed by Drits et al. (1997), the maximum possible Na^+ and Mn^{3+} content in NaBu is given by the formula $Na^+_{0.33}Mn^{4+}_{0.67}Mn^{3+}_{0.33}O_{\sim 2}$, because an Na^+ content greater than this requires Na^+-Na^+ pairs at distances of 2.85 Å. It appears reasonable to conclude that the experimentally determined chemical formula in which the Mn^{2+} content is assumed to be zero, $Na^+_{0.3}Mn^{4+}_{0.69}Mn^{3+}_{0.31}O_{\sim 2}$, gives the best chemical description of NaBu, corresponding almost to the maximum Mn^{3+} and Na^+ content possible. It is most likely that the process of drying NaBu to form NaBi results in the disproportionation of some Mn^{3+} (approximately one-third), according to the $\lambda = 6b$ periodicity along Mn^{3+}-rich rows (Drits et al. 1997), and the migration of Mn^{2+} into the interlayer region, yielding the chemical formula: $Na^+_{0.3}Mn^{2+}_{0.049}(Mn^{4+}_{0.739}Mn^{3+}_{0.212}\square_{0.049}O_{\sim 2})$, where $\square$ represents a layer vacancy. SAED studies (Drits et al. 1997) show that for the more dominant of the microcrystal types observed for NaBi (type II) the idealized chemical formula is $Na^+_{0.33}Mn^{2+}_{0.055}(Mn^{4+}_{0.722}Mn^{3+}_{0.222}\square_{0.055}O_{\sim 2})$. Clearly there is very good agreement between this chemical formula and that measured experimentally when the maximum possible content of Mn^{2+} is assumed. The results from the polarized EXAFS measurements on NaBi indicate the absence of TC-sharing Mn in this mineral. This result would strongly indicate that Mn^{2+} that migrates into the interlayer does not reside at layer vacancy sites, although the few Mn^{2+} cations involved forces us to be less conclusive on this point.

Implicit in the development of a structural formula for NaBi is the conclusion that the quantity of Mn^{2+} that is observed in solution upon conversion of NaBu to HBi is the same as that which exists within the structure of NaBi. The strong correlation between the solution level of Mn^{2+} observed at pH < 2, corresponding to one-twentieth of the total Mn, with that expected from the $\lambda = 6b$ periodicity of one-eighteenth of total Mn, supports this interpretation. Put another way, it appears from the results of this study that both the conversion of NaBu to NaBi by means of dehydration and the conversion of NaBu to HBi at low pH result in an equivalent amount of layer Mn^{3+} disproportionation.

Structure of HBi

There appears to be a close similarity between chalcophanite and HBi, based on the evidence from the XRD (Drits et al. 1997) and EXAFS results, which demonstrate the existence of TC-sharing Mn cations located on lattice vacancy sites. The Mn-Mn TC-sharing peak is observed for all HBi samples. Given that there is no re-adsorption of Mn^{2+} at pH 2 (Fig. 2) during the structural alteration of NaBu, part of the TC-sharing component must come from a direct structural re-arrangement of the MnO_6 edge-sharing layers. This observation, combined with the observed change between a distorted hexagonal layer structure for NaBi and an undistorted layer structure for HBi, suggests that upon lowering the pH, there is a significant migration of lower valence Mn into the interlayer region. This conclusion is also in accord with the observed decrease in the Mn-Mn edge-sharing distance between NaBi and HBi. The results of polarized EXAFS for HBi have shown that Mn adsorbed at lattice vacancy sites has a smaller ionic radius than Zn^{2+} and is therefore dominantly Mn^{3+} or Mn^{4+}. Quite clearly, any mechanism of NaBu to HBi conversion in which the migration of Mn^{4+} from layer to TC-sharing positions occurs, would result in a relative increase in the lower valence content of the layers, in total contradiction of the experimental data. For this reason, the results obtained by polarized EXAFS must be interpreted as evidence for a dominance of Mn^{3+} adsorbed on layer vacancies in HBi.

As discussed by Drits et al. (1997), HBi microcrystals exhibit a weak superstructure, with the unit-cell parameters $A = 3a$ and $B = b$. This superstructure was interpreted as arising from the distribution of layer vacancies and associated TC-sharing Mn cations. Manganese cations coordinated to vacancy sites would also be associated with three interlayer H_2O molecules, resulting in an enhanced scattering intensity in the *a*-*b* plane. This interpretation of the superstructure in HBi leads to the conclusion that lattice vacancies are restricted to the rows that originally contained Mn^{3+} in NaBu and NaBi, i.e., every third row running along the [010] direction.

From the EXAFS data obtained for HBi prepared at pH 5, which has the maximum number of TC-sharing and minimum number of edge-sharing Mn, it is possible to estimate

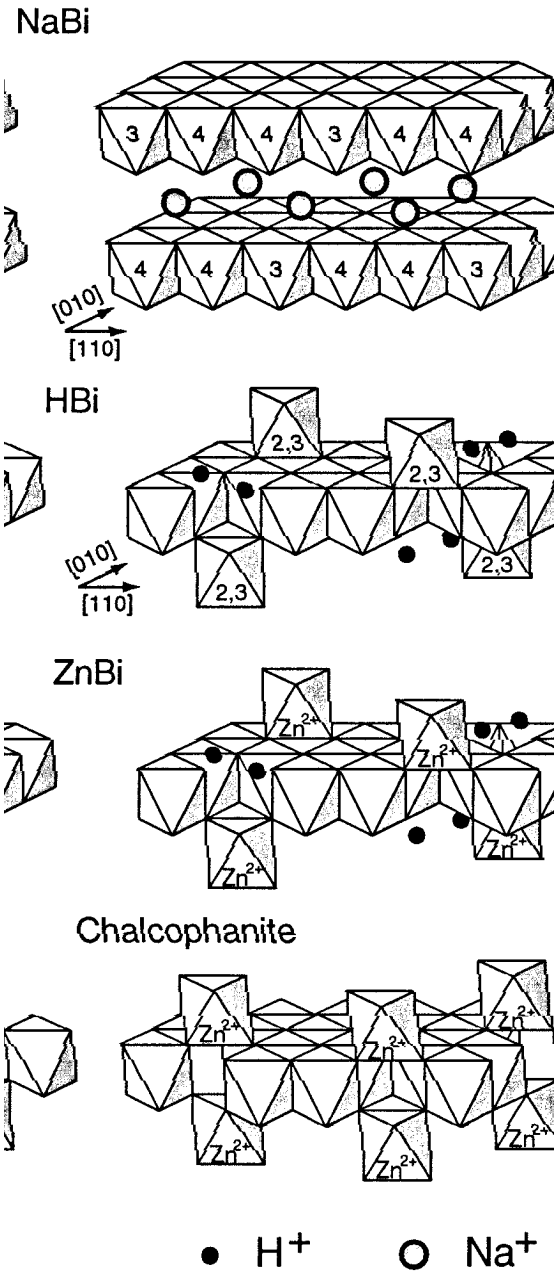

FIGURE 11. Proposed structural models for NaBi, HBi, and ZnBi as determined from the results of this study. The numbers on the faces of the octahedra in the NaBi structure refer to the sequence of Mn valency in the [110] or [10] directions. The numbers on the TC-sharing octahedra in the HBi structure indicate that a mixture of Mn^{3+} and Mn^{2+} cations occupy these sites. Also shown is a structural model for chalcophanite from Wadsley (1955) and Post and Appleman (1988).

the density of vacancies in the layers. The outcome of this calculation depends on the assumed vacancy distribution in the layers. For the reasons given above, vacancies are assumed to be restricted to every third row in the [010] direction. If all Mn^{3+} cations along the Mn^{3+}-rich rows of NaBu were to migrate from layer to interlayer positions, the expected numbers of TC-sharing and edge-sharing neighbors in the EXAFS fitting procedures would be 2.7, for both distances. The experimental values of $N_{TC} = 2.0$ and $N_E = 4.1$ for HBi at pH 5 clearly demonstrate that not all of the Mn^{3+} cations migrate from the layers. It is readily shown that these experimental values in fact correspond closely to that expected where there is a 50% density of vacancies in these rows, with every layer vacancy having an associated TC-sharing Mn. The theoretical number of TC- and edge-sharing neighbors corresponding to this cation distribution is 2.0 and 4.0, respectively.

It would appear that there are two principal mechanisms of TC-sharing Mn formation in HBi. One involves the direct migration of Mn^{3+} from the layer to the interlayer and the second the adsorption of Mn^{2+} from solution onto lattice vacancy sites. This second mechanism explains the increase in the TC-sharing distance and amplitude with increasing pH for the HBi series of samples. At pH 5 the re-adsorption of Mn^{2+} results in complete occupancy of the vacancy sites, consistent with the number of edge- and TC-sharing neighbors for this sample, whereas at pH 2 no re-adsorption of Mn^{2+} occurs. Within the framework of this model, two extreme cation distributions for the HBi series of samples can be identified. All HBi samples have a vacancy density of 50% along every third cation row. At pH 2, 67% of vacancy sites have an associated TC-sharing Mn and all are Mn^{3+}. At pH 5 there is 100% occupancy of the lattice vacancies, with a valency distribution of 67% Mn^{3+} and 33% Mn^{2+}. This model is consistent with a dominance of Mn^{3+} in TC-sharing positions under all pH conditions.

Because all Na^+ is lost from the interlayer region upon forming HBi, layer-layer stabilization must occur by means of hydrogen bonding by TC-sharing Mn ions with adjacent layers, similar to that observed for chalcophanite. This model of the interlayer structure provides an explanation for the change in interlayer spacing from 10 Å for NaBu to 7 Å for HBi. One important difference between HBi and chalcophanite is that in the latter mineral Zn^{2+} cations occur in pairs at lattice vacancies whereas the evidence here suggests that this does not occur in HBi. The absence of a peak at 4.1 Å in the RDF of ZnBi shown in Figure 4 indicates that there are also very few pairs of Zn^{2+} cations at layer vacancy sites for this synthetic phase. In this sense ZnBi is very similar to HBi, which suggests that the mechanism of HBi to ZnBi conversion proceeds by means of displacement of Mn cations adsorbed at layer vacancies by Zn^{2+} cations. The reason for the absence of cation pairs across layer vacancies in HBi and ZnBi is not clear from the results of this study, but it is possibly related to the distribution of lattice vacancies in the layers.

Diagrams of the structures of NaBi, HBi, and ZnBi, as determined from the results of this study, are shown in Figure 11. Also shown in this figure, for purposes of comparison, is the structure of chalcophanite from the results of previous studies (Post and Appleman 1988; Wadsley 1955).

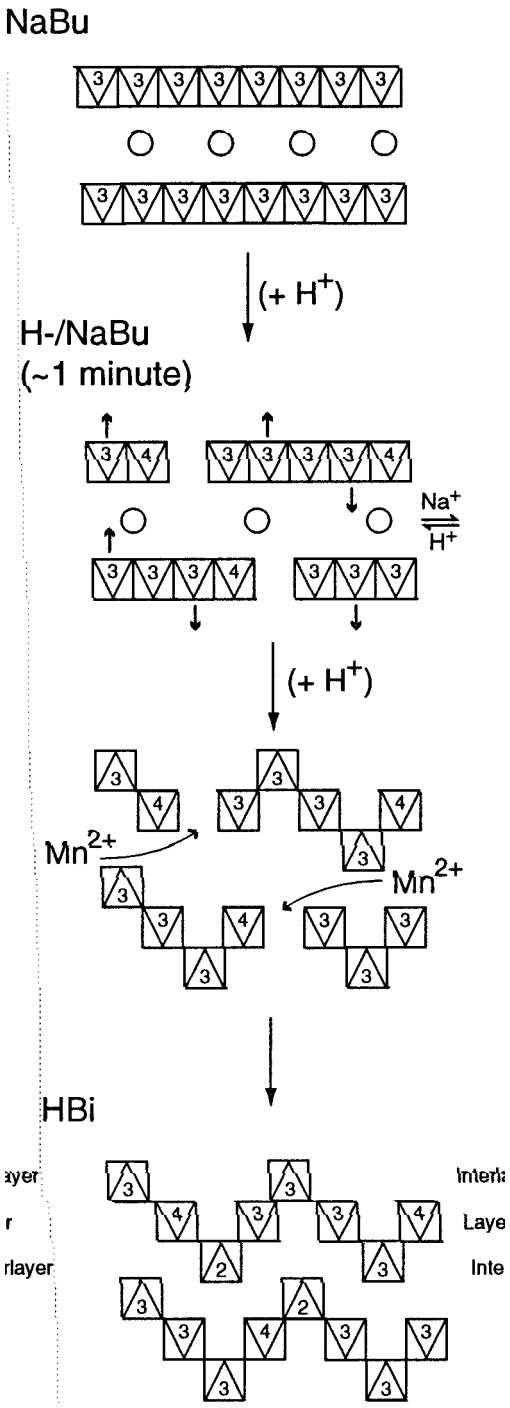

FIGURE 12. Schematic diagram showing the changes in cation layer and interlayer positions along the Mn^{3+}-rich rows for the alteration of NaBu to HBi at low pH. Mn^{4+}-rich rows are assumed to be unaffected by the structural alteration at low pH. This diagram shows: (1) the partial loss of Na^+ from the interlayers and the partial disproportionation of layer Mn^{3+}, according to $\lambda = 6b$ periodicity, (2) the migration of layer Mn^{3+} into interlayer (TC-sharing) positions (creating a vacancy density of 50% along these rows) and the desorption of the remaining interlayer Na^+, and (3) re-adsorption of solution Mn^{2+} onto available layer-vacancy sites, as controlled by the solution pH. Large open circles symbolize Na^+ cations, and the numbers on the octahedra correspond to the Mn valency.

→

Mechanism of the NaBu-to-HBi conversion

Figure 12 shows a schematic sequence for the conversion of NaBu to HBi that allows an understanding of both the chemical and structural observations. According to the proposed model, NaBu is a layered material containing only Mn^{4+} and Mn^{3+} in the layer with no layer vacancies and hence no TC-sharing interlayer Mn cations. NaBu undergoes a rapid partial equilibration under low pH conditions resulting in a redistribution of layer and interlayer cations. One-third of the Mn^{3+} (corresponding to the $\lambda = 6b$ periodicity) disproportionates to form Mn^{4+}_{layer} and Mn^{2+}, with the latter migrating into the solution phase. A significant proportion of the Na^+ (~two-thirds) remains associated with the solid. This heterogeneity in the binding strength of interlayer Na^+ correlates well with the results presented by Drits et al. (1997). For the type II microcrystals of NaBi, approximately one-third of all interlayer Na^+ is associated exclusively with layer Mn^{4+}, and hence only weakly bound to the layers. It seems most likely that these Na^+ ions exchange rapidly with solution H^+ at low pH. The Na^+ that remains in the interlayer after the initial rapid process therefore corresponds to Na^+ associated with layer Mn^{3+}. The chemical formula of the intermediate H-NaBu phase created can be written as: $Na^+_{0.19}[Mn^{4+}_{0.739}Mn^{3+}_{0.212}\square O_{1.79}(OH)_{0.21}]$. In this formula no attempt was made to account for any hydroxide groups that may have been present initially in the NaBu structure, although these should be very few.

In the subsequent slow exchange process the remaining Na^+ desorbs, with the layer charge balanced by the adsorption of Mn^{2+} and H^+ in proportions that depend on the solution pH. The observation that Na^+ desorbs from NaBu regardless of whether Mn^{2+} re-adsorbs indicates that the mechanism of Na^+ desorption does not involve Mn^{2+}. For this reason it appears most likely that the slow Na^+ desorption step relates to a structural re-arrangement of the solid, probably mediated by solution H^+. The nature of this structural re-arrangement is unclear. One possible mechanism is that the migration of Mn^{3+} from the layer to interlayer positions occurs slowly. Only after the formation of TC-sharing Mn does the exchange of adsorbed Na^+ with solution H^+ becomes energetically favorable.

Symmetry of the phyllomanganate layers

From the results of powder and polarized EXAFS measurements, combined with the SAED results (Drits et al. 1997), we show that lattice vacancies in HBi are predominantly restricted to every third cation row in the layers. This distribution of vacancies appears to be a vestige of the original Mn^{3+} distribution in NaBu and NaBi. The vacancy density within these rows is close to 50% cor-

responding to a total vacancy density in the layers of one in six of all Mn sites. Both the occupancy of lattice vacancy sites by TC-sharing Mn cations and the valence distribution of the adsorbed Mn appear to be pH dependent. The model developed for the structure of HBi requires that some Mn^{3+} cations remain in the layers. This conclusion is unequivocal given that there is no change in the average oxidation state of Mn during the conversion of NaBu to NaBi. Assuming that these layer Mn^{3+} cations are restricted to the vacancy-rich rows, one-third of the available cation sites in these rows must be occupied by Mn^{3+}, equivalent to one in nine of all layer cation sites. This quantity of Mn^{3+} is apparently insufficient to cause a distortion of the hexagonal layer symmetry. Several studies have reported the structural and electrochemical properties of γ-MnOx as a function of the degree of Mn oxidation (e.g., Giovanoli and Leuenberger 1969; Ruetschi 1984; Chabre and Pannetier 1995). It is generally observed that the structural and electronic properties of γ-MnOx change dramatically about the mid-point between pure Mn^{3+} and Mn^{4+} oxide materials, i.e., about $x = 1.75$ in MnOx. At degrees of Mn oxidation greater than this, bulk Jahn-Teller distortion of the structure is not observed. This observation was explained in terms of the random distribution and directional orientation of Mn^{3+} centers throughout the structure. In considering the electronic and structural difference between NaBi and HBi it is important to distinguish between the oxidation state of the layers and the oxidation state of the solid as a whole, which does not change between NaBu or NaBi and HBi. Taking into account the lattice vacancy density of one in six and the Mn^{3+} abundance in the vacancy-rich rows of 33% in HBi, it is readily calculated that, whereas the layers of NaBi correspond to an MnOx solid with $x = 1.845$, in HBi the layers correspond to $x = 1.94$. Put another way, the migration of Mn^{3+} from the layer to the interlayers effectively results in an oxidation of the layers. This greatly reduced proportion of Mn^{3+} in the layers of HBi is consistent with a reduction (quasi-absence) of layer distortion. An additional factor involved in the electronic distribution of NaBi and HBi is that compensation of the layer charge is achieved by Na^+ and H^+, respectively. It is reasonable to assume that the interlayer mobility of Na^+ is considerably lower than that for protons, on the basis of both the ion sizes and the existence of the chain mechanism for proton diffusion. It is most likely that both the migration of lower valence Mn to the interlayer region and the change in the interlayer speciation from Na^+ to H^+ are contributing factors in the change between the monoclinic symmetry of NaBi and the hexagonal symmetry of HBi. The structural modification that occurs at low pH results in two principal effects that provide a more energetically favorable situation. First, the removal of lower valence Mn from the layer relieves the steric strain associated with the presence of Mn^{3+} rows. Second, the formation of TC-sharing Mn atoms creates an interlayer structure that stabilizes the layer-layer distance in HBi.

Acknowledgments

The authors thank R. Giovanoli who advised us on the preparation of Na-rich birnessite and more generally on the properties of this material. We also thank the staff at L.U.R.E. for operating the synchrotron facility. We were kindly assisted by Bruno Lanson in the preparation of this manuscript in its final form.

References cited

Baes, C.F. and Mesmer, R.E. (1976) The hydrolysis of cations. p. 219–226. Wiley, New York.

Burns, R.G. and Burns, V.M. (1977) The mineralogy and crystal chemistry of deep-sea manganese nodules, a polymetallic resource of the twenty-first century. Philosophical Transactions of the Royal Society of London (A), 286, 283–301.

Brouder, C. (1990) Angular dependence of X-ray absorption spectra. Journal of Physics, 2, 701–738.

Crowther, D. L., Dillard, J.G., and Murray, J.G. (1983) The mechanism of Co(II) oxidation on synthetic birnessite. Geochimica et Cosmochimica Acta, 47, 1399–1403.

de Wolff, P.M. (1959) Interpretation of some γ-MnO_2 diffraction patterns. Acta Crystallographica, 12, 341–345.

Drits, V.A., Silvester, E., Gorshkov, A.I., and Manceau, A. (1997) The structure of monoclinic Na-rich birnessite and hexagonal birnessite: I. Results from X-ray diffraction and selected-area electron diffraction. American Mineralogist, 82, 946–961.

Freeman, D.S. and Chapman, W.G. (1971) An improved oxalate method for the determination of active oxygen in manganese dioxide. Analyst, 96, 865–869.

Giovanoli, R. (1980) On natural and synthetic manganese nodules. In J.M. Varenstov and J. Grasselly, Eds., Geology and geochemistry of manganese, vol. 1, p. 154–202. Academia Kiado, Budapest.

Giovanoli, R. and Leuenberger, U. (1969) Über die Oxydation von Manganoxidhydroxid. Helvetica Chimica Acta, 52, 2333–2347.

Giovanoli, R., Stähli, E., and Feitknecht, W. (1970a) Über Oxidhydroxide des vierwertigen Mangans mit Schichtengitter. 1. Mitteilung: Natriummangan(II,III)manganat(IV). Helvetica Chimica Acta, 53, 454–464.

——— (1970b) Über Oxidhydroxide des vierwertigen Mangans mit Schichtengitter. 2. Mitteilung: Mangan(III)-manganat(IV). Helvetica Chimica Acta, 53, 454–464.

Gray, M.J. and Malati, M.A. (1979a) Adsorption from aqueous solution by δ-manganese dioxide. I. Adsorption of the Alkaline-earth cations. Journal of Chemical Technology and Biotechnology, 29, 127–134.

——— (1979b) Adsorption from aqueous solution by δ-manganese dioxide. II. Adsorption of some heavy metal cations. Journal of Chemical Technology and Biotechnology, 29, 135–144.

Hazemann, J.L., Manceau, A., Sainctavit, P., and Malgrange, C. (1992) Structure of the αFexAl$_{1-x}$OOH solid solution. I. Evidence by polarized EXAFS for an epitaxial growth of hematite-like clusters in diaspore. Physics and Chemistry of Minerals, 19, 25–38.

Heald, S.M. and Stern, E.A. (1977) Anisotropic x-ray absorption in layered compounds. Physical Review B, 16, 5549–5559.

Kolthoff, I.M. and Sandell, E.B. (1952) Textbook of Quantitative Inorganic Analysis (3rd edition), p. 681. Macmillan, New York.

Krauskopf, K.B. (1957) Separation of manganese from iron in sedimentary processes. Geochimica et Cosmochimica Acta, 12, 61–84.

Kuma, K., Usui, A., Paplawsky, W., Gedulin, B., and Arrhenius, G. (1994) Crystal structures of synthetic 7 Å and 10 Å manganates substituted by mono- and divalent cations. Mineralogical Magazine, 58, 425–447.

Manceau, A. (1995) The mechanism of anion adsorption on iron oxides: Evidence for the bonding of arsenate tetrahedra on free Fe(O,OH)$_6$ edges. Geochimica et Cosmochimica Acta, 59, 3647–3653.

Manceau, A. and Combes, J.M. (1988) Structure of Mn and Fe oxides and oxyhydroxides: a topological approach by EXAFS. Physics and Chemistry of Minerals, 15, 283–295.

Manceau, A. and Gates, W.P. (1997) Surface structural model for ferrihydrite. Clays and Clay Minerals, in press.

Manceau, A., Bonnin, D., Kaiser, P., and Frétigny, C. (1988) Polarized EXAFS of biotite and chlorite. Physics and Chemistry of Minerals, 16, 180–185.

Manceau, A., Bonnin, D., Stone, W.E.E., and Sanz, J. (1990) Distribution of Fe in the octahedral sheet of trioctahedral micas by polarized EXAFS. Comparison with NMR results. Physics and Chemistry of Minerals, 17, 363–370.

Manceau, A. and Charlet, L. (1992) X-ray absorption spectroscopic study of the sorption of Cr(III) at the oxide-water interface. Journal of Colloid and Interface Science, 148, 425–442.

Manceau, A., Gorshkov, A.I., and Drits, V.A. (1992) Structural chemistry of Mn, Fe, Co, and Ni in manganese hydrous oxides: II. Information from EXAFS spectroscopy and electron and X-ray diffraction. American Mineralogist, 77, 1144–1157.

McKenzie, R.M. (1967) The sorption of cobalt by manganese minerals in soils. Australian Journal of Soil Research, 5, 235–246.

——— (1980) The adsorption of lead and other heavy metals on oxides of manganese and iron. Australian Journal of Soil Research, 18, 61–73.

O'Day, P.A., Rehr, J.J., Zabinsky, S.I., and Brown, G.E. (1994) Extended x-ray absorption fine structure (EXAFS) analysis of disorder and multiple-scattering in complex crystalline solids. Journal of the American Chemical Society, 116, 2938–2949.

Post, J.E. and Appleman, D.E. (1988) Chalcophanite, $ZnMn_3O_7 \cdot 3\ H_2O$: New crystal structure determinations. American Mineralogist, 73, 1401–1404.

Post, J.E. and Veblen, D.R. (1990) Crystal structure determinations of synthetic sodium, magnesium, and potassium birnessite using TEM and the Rietveld method. American Mineralogist, 75, 477–489.

Ruetschi, P. (1984) Cation-vacancy model for MnO_2. Journal of the Electrochemical Society, 131, 2737–2744.

Shuey, R.T. (1975) Developments in economic geology, 4. Semiconducting ore minerals, p. 389–396. Elsevier, Amsterdam.

Stern, E.A. and Heald, S.M. (1983) Basic principles and applications of EXAFS. In E. Koch, Ed., Handbook on synchrotron radiation, Amsterdam, North Holland p. 955–1014.

Stern, E.A. and Kim, K. (1981) Thickness effect on the extended x-ray absorption fine structure amplitude. Physical Review B, 23, 3781–3787.

Strobel, P., Charenton, J.C., and Lenglet, M. (1987) Structural chemistry of phyllomanganates: experimental evidence and structural models. Revue de Chimie Minérale, 24, 199–220.

Teo, B.K. (1986) EXAFS: Basic principles and data analysis, 349 p. Springer-Verlag, Berlin.

Teo, B.K. and Lee, P.A. (1979) Ab initio calculations of amplitude and phase functions for extended X-ray absorption fine structure spectroscopy. Journal of the American Chemical Society, 101, 2815–2832.

Thackeray, M.M., de Kock, A., and David, W.I.F. (1993) Synthesis and structural characterisation of defect spinels in the lithium-manganese-oxide system. Material Research Bulletin, 28, 1041–1049.

Turner, S. and Post, J.E. (1988) Refinement of the substructure and superstructure of romanechite. American Mineralogist, 73, 1155–1161.

Wadsley, A.D. (1953) The crystal structure of psilomelane, $(Ba, H_2O)_2Mn_5O_{10}$. Acta Crystallographica, 6, 433–438.

——— (1955) The crystal structure of chalcophanite, $ZnMn_3O_7.3\ H_2O$. Acta Crystallographica, 8, 165–172.

Werhli, B., Friedl, G., and Manceau, A. (1995) Reaction rates and products of manganese oxidation at the sediment-water interface. In C.P. Huang, C.R. O'Melia, and J.J. Morgan, Eds., Advances in chemistry series No. 244, Aquatic chemistry: Interfacial and interspecies processes. American Chemical Society, Washington.

Xyla, A.G., Sulzberger, B., Luther, G.W., Hering, J.G., Van Capellen, P., and Stumm, W. (1992) Reductive dissolution of manganese(III,IV) (hydr)oxides by oxalate: The effect of pH and light. Langmuir, 8, 95–103.

Manuscript received June 21, 1996
Manuscript accepted May 23, 1997